

Design and commissioning of a timestamp-based data acquisition system for the DRAGON recoil mass separator

G. Christian¹ ^a, C. Akers^{1,2}, D. Connolly³, J. Fallis¹, D. Hutcheon¹, K. Olchanski¹, and C. Ruiz¹

¹ TRIUMF, 4004 Wesbrook Mall, Vancouver, BC V6T 2A3, Canada

² Department of Physics, University of York, Heslington, York YO10 5DD, UK

³ Department of Physics, Colorado School of Mines, 1523 Illinois Street, Golden, CO 80401, USA

Received: / Revised version:

Abstract. The DRAGON recoil mass separator at TRIUMF exists to study radiative proton and alpha capture reactions, which are important in a variety of astrophysical scenarios. DRAGON experiments require a data acquisition system that can be triggered on either reaction product (γ ray or heavy ion), with the additional requirement of being able to promptly recognize coincidence events in an online environment. To this end, we have designed and implemented a new data acquisition system for DRAGON which consists of two independently triggered readouts. Events from both systems are recorded with timestamps from a 20 MHz clock that are used to tag coincidences in the earliest possible stage of the data analysis. Here we report on the design, implementation, and commissioning of the new DRAGON data acquisition system, including the hardware, trigger logic, coincidence reconstruction algorithm, and live time considerations. We also discuss the results of an experiment commissioning the new system, which measured the strength of the $E_{c.m.} = 1113$ keV resonance in the $^{20}\text{Ne}(p, \gamma)^{21}\text{Na}$ radiative proton capture reaction.

PACS. 29.85.Ca Data acquisition, nuclear physics – 25.40.Lw Radiative capture

1 Introduction

1.1 The DRAGON Facility

Radiative capture reactions typically involve the absorption of a light nucleus (typically a proton or an α particle) by a heavy one, followed by γ -ray emission. These reactions are important in a variety of astrophysical scenarios such as novae [1, 2, 3, 4, 5, 6], supernovae [7], X-ray bursts [8, 9], and quiescent stellar burning [10, 11]. They are often difficult to study directly in the laboratory. The cross sections are low, typically on the order of picobarns to millibarns, since the relevant energies are below the Coulomb barrier. Additionally, many interesting reactions involve short-lived nuclei and can only be studied using low-intensity radioactive beams.

The Detector of Recoils and Gammas of Nuclear Reactions (DRAGON) facility at TRIUMF [12], shown in Fig. 1, is a recoil mass separator that was built to study radiative capture reactions using stable and radioactive beams from the ISAC-I [13] facility. DRAGON experiments are typically performed in inverse kinematics with a beam of the heavy nucleus impinging on a windowless gas target containing the lighter one. Beam energies range from $E/A = 0.15$ – 1.5 MeV. The products of radiative capture (recoils) are transmitted through DRAGON and detected

in a series of charged particle detectors, while unreacted beam and other products are deposited at various points along the separator's flight path. The recoil detectors consist of a pair of microchannel plates (MCPs) to measure local time of flight (TOF) [14] and either a double-sided silicon strip detector (DSSSD) [15] or an ionization chamber (IC) to measure energy loss. The γ rays resulting from radiative capture are detected in an array of 30 bismuth germanate (BGO) detectors surrounding the target.

For beam normalization, the target chamber houses two ion-implanted silicon (IIS) detectors to record elastically scattered target nuclei. In a typical experiment, the scattering rates measured in the IIS detectors are normalized to hourly Faraday cup readings of the absolute beam current. Experiments using low-intensity and possibly unpure radioactive beams may also include a pair of sodium iodide (NaI) scintillators, a high purity germanium (HPGe) detector, or both. These auxiliary detectors are located near the first mass-dispersed focus, and they detect the γ rays resulting from the decay of radioactive beam deposited onto the nearby slits. This allows a continuous determination of the beam rate and composition throughout the experiment.

In many experiments, unreacted, scattered, or charge-changed beam particles (“leaky beam”) are transmitted to the end of DRAGON along with the recoils of interest. The rates vary depending on experimental conditions but

^a gchristian@triumf.ca

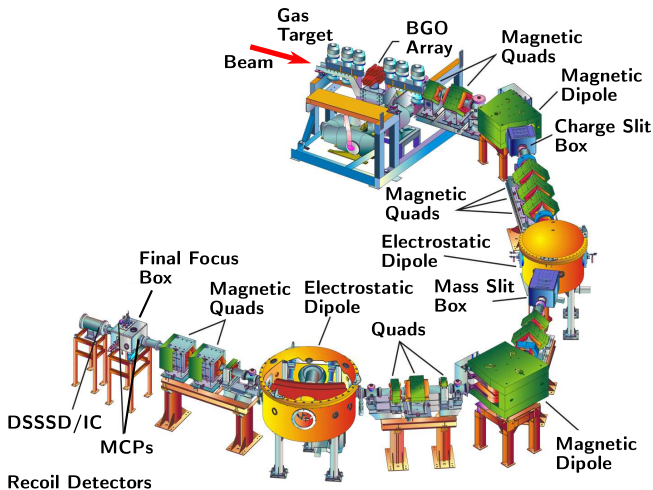


Fig. 1. The DRAGON facility at TRIUMF.

can potentially be as much as a few thousand times the recoil rate [16]. Hence, it is crucial that leaky beam be separable from recoils in the data analysis. In some cases, separation is possible using the signals from recoil detectors alone. In others, it is necessary to require (delayed) coincidences between the heavy ion and a γ ray measured in the BGO detectors. In such experiments, a measurement of the TOF between the γ ray and the heavy ion (“separator TOF”) is useful for distinguishing genuine coincidences from random background.

1.2 Data Acquisition Requirements

As mentioned, identification of coincidences between the “head” (γ -ray) and “tail” (heavy-ion) detectors is important for many DRAGON experiments. As a result, the original DRAGON data acquisition (DAQ) was designed to trigger on singles events from either detector system while also identifying coincidences from hardware gating. The resulting trigger logic was rather complicated and required a moderate amount of hardware reconfiguration when changing the detector setup (for example, swapping the DSSSD and IC). With this system, the potential for logic problems due to human error or faulty modules was relatively high, resulting in the possibility of wasted beam time or otherwise non-optimal data sets.

In order to alleviate the problems associated with the existing coincidence logic, we have designed and implemented a new DAQ system for DRAGON that identifies coincidences from timestamps instead of hardware gating. In the course of doing this, we have also upgraded the digital readout from a computer automated measurement and control (CAMAC) system to VERSAmodule Eurocard (VME) and migrated part of the trigger logic from nuclear instrumentation module (NIM) hardware to a field-programmable gate array (FPGA). In the new setup, the head and tail systems are triggered and read out completely independent of each other, and coincidences

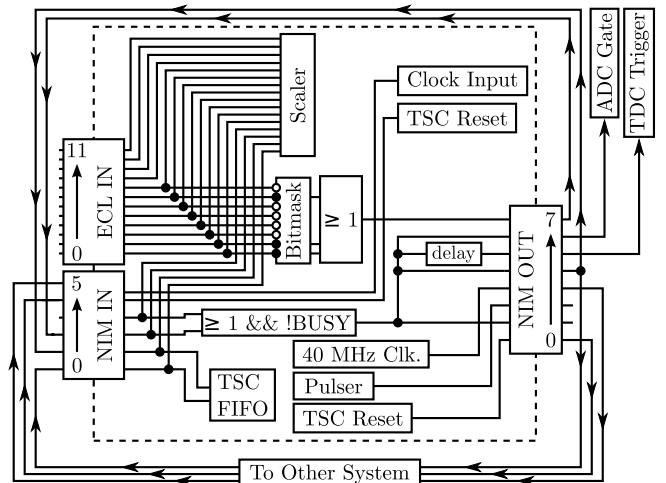


Fig. 2. Diagram of the generic IO32 FPGA logic. See the text for further explanation.

are identified in the analysis stage from timestamp matching.

In this paper, we provide an overview of the new DRAGON DAQ system and data analysis codes. We also discuss the results of the DAQ commissioning experiment, which consisted of a measurement of the $E_{c.m.} = 1113$ keV resonance strength in the $^{20}\text{Ne}(p, \gamma)^{21}\text{Na}$ radiative proton capture reaction.

2 Trigger Logic

The majority of the DRAGON trigger logic and timestamping functionality is implemented in FPGA firmware. For this we use an IO32, a general purpose VME board designed and manufactured at TRIUMF [17]. The IO32 houses an Altera Cyclone-I FPGA [18] and has input-output capabilities via sixteen NIM and sixteen emitter coupled logic (ECL) input channels and sixteen NIM outputs. It also houses a 20 MHz quartz oscillator crystal with an accuracy rating of 20 parts per million.

The FPGA logic is designed in a generic way, allowing identical firmware to be used for both the head and tail systems. A diagram of the FPGA logic is shown in Fig. 2. ECL inputs 0–11 accept trigger signals from various detectors and are all routed into a firmware scaler for rate counting, as are NIM inputs 0–3. ECL inputs 0–8 are also sent through a programmable bitmask, and the OR of the unmasked channels is sent to NIM output 7 which is then routed into either NIM input 2 or NIM input 3. The OR of NIM input 2 and NIM input 3 is combined with an internal NOT BUSY condition to generate a system trigger. This causes a logic pulse to be emitted from NIM output 4, and this is then routed back into NIM input 1 which tells the system to begin acquiring data. The input of NIM input 1 is also sent to a first in, first out (FIFO) data structure that stores the timestamp counter (TSC) value denoting when the signal arrived. These data are used for coincidence matching in the analysis stage, as explained

in Sect. 3.1. The signal from NIM output 4 is also sent to the other system (head to tail or vice-versa). There it is connected to NIM input 0 which is also routed into the TSC FIFO.

A system trigger also results in signals being sent from NIM outputs 1, 5, and 6. NIM output 1 emits a “busy” signal that remains true until cleared by a VME register setting. This signal is not necessary to run the system, but it is often useful for debugging purposes. NIM output 5 emits a logic pulse after a programmable time delay. This pulse is sent to the system’s time to digital converter (TDC) to act as the stop signal¹. NIM output 6 emits a pulse of programmable width which is used to gate the system’s amplitude to digital converter (ADC) or charge to digital converter (QDC). The IO32 firmware also includes a programmable pulse generator. This is a square wave of programmable frequency emitted from NIM output 2.

The TSC is run off a clock with 20 MHz nominal frequency. Its size is 38 bits, allowing ~ 3.8 hours of run time before it rolls over. The acquisition software also keeps track of any roll over in the 38-bit counter, allowing the system to run indefinitely. The exact clock frequency is set either by the quartz crystal housed on the IO32 board or by a signal with two times the desired clock frequency (i.e., a nominal frequency of 40 MHz) sent into NIM input 5. The TSC value can be reset to zero either by writing to a VME register or by sending a pulse to NIM input 4. Zeroing by the VME method causes a signal to simultaneously be emitted from NIM output 0. Multiple boards can be run in master-slave configuration where the master is clocked off its local quartz oscillator and the slave(s) are clocked off the 40 MHz output of the master. In this setup, the master clock is zeroed by VME and the slave(s) by a pulse sent from NIM output 0 of the master. The result is a frequency synchronization and zero-point matching which differs only by the transit time of the zero-reset pulse (which is typically negligible). The DRAGON system is run in such a master-slave configuration, with the head IO32 arbitrarily designated the master and the tail the slave.

A diagram of the specific trigger logic used in the DRAGON head and tail systems is shown in Fig. 3. On the head side, the anode signals from the 30 BGO detectors are split into analog and logic branches. The analog branch is sent through a physical time delay before going to the input of a CAEN V792 QDC [20]. The length of the time delay is set such that the signals arrive at the QDC more than 15 ns after the leading edge of the gate pulse, as required by the QDC specifications. Signals in the logic branch are sent to a pair of CAEN V812 constant fraction discriminators (CFDs) [21]. The channel-by-channel CFD outputs are sent to the inputs of a CAEN V1190 TDC [19], and the OR outputs are sent to ECL input 0 and ECL input 1 to generate the system trigger and associated signals (QDC gate and TDC trigger). A copy of the system trig-

¹ In reality, it is not a “stop” that is sent to the TDC, but rather a “trigger” signal that must come after all of the measurements in the corresponding event. See Ref. [19] for more details.

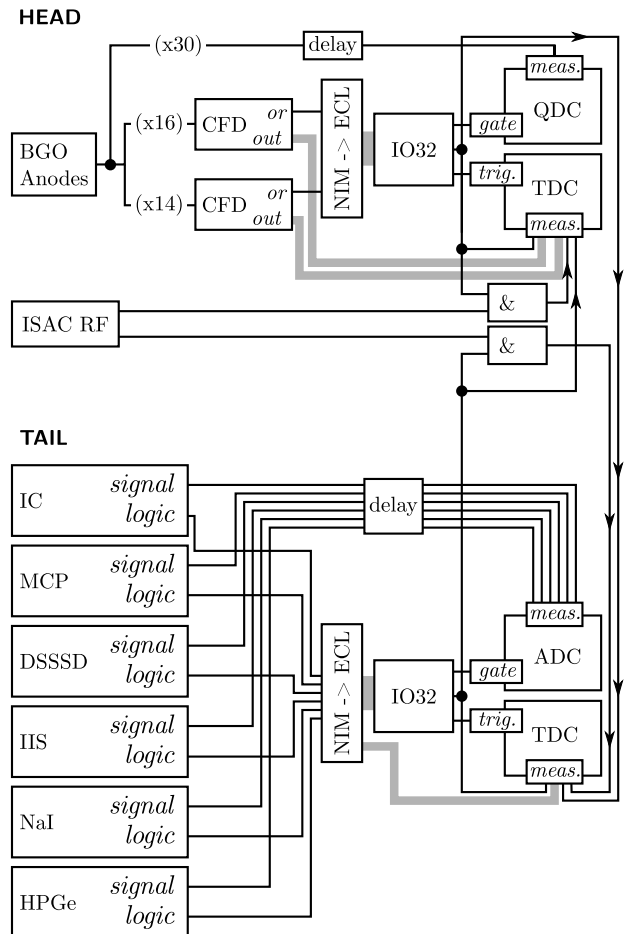


Fig. 3. Diagram of the timestamp-based DRAGON trigger logic. See the text for more explanation.

ger is sent to a measurement channel of both the head and tail TDCs, to facilitate a measurement of separator TOF.

On the tail side, the trigger is essentially an OR of each of the heavy-ion detectors mentioned in Sect. 1.1. The outputs of each heavy-ion detector are sent through some combination of amplifiers, shapers, and discriminators (whose exact configuration varies and is outside the scope of this paper) until there is an analog signal suitable for amplitude measurement and a digital signal suitable for triggering and timing. The analog signals are sent to the inputs of a CAEN V785 ADC [22], possibly after a physical time delay to place them within the ADC gate. The logic signals are sent to measurement channels of a CAEN V1190 TDC and to ECL inputs 0–7 to create the system trigger, ADC gate, and TDC trigger signals. As with the head system, a copy of the system trigger is sent to measurement channels of both the head and tail TDCs, resulting in a redundant measurement of separator TOF. In some cases, logic signals from detectors that measure incoming beam rates or composition (IIS, NaI, and HPGe) may be downscaled to reduce the total trigger rate and, correspondingly, the dead time.

In both systems, a copy of the 11.8 MHz ISAC-I radio frequency quadrupole (RF) accelerator signal is sent to

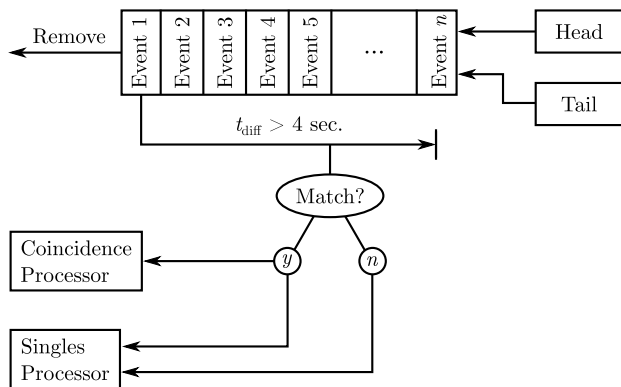


Fig. 4. Diagram of the coincidence matching algorithm. See the text for more information.

the TDC to be used as an additional timing reference. To avoid swamping the TDC buffers with RF pulses, the signal is gated by an adjustable-width copy of the system trigger. Typically, the gate width is set large enough that three full RF pulses are captured for every event.

3 Data Acquisition and Analysis

The data acquisition and online data analysis codes are both implemented as part of the Maximum Integrated Data Acquisition System (MIDAS) framework [23]. The acquisition code is implemented in C++ and employs device driver codes that are widely used at TRIUMF [24]. MIDAS transition handler priorities are used to specify the order of head and tail initialization routines at the beginning of each data-taking run. This ensures that operations which are required for timestamp matching, such as TSC zeroing, are performed in the necessary order.

The analysis codes are also written in C++ and are designed such that they can be used for both online and offline analysis using the ROOT data analysis framework [25]. Each individual detector in the system is represented in a C++ class, with data fields corresponding to the available measurement parameters. The various detectors in the head and tail systems are then composed into a larger class. For coincidence events, the head and tail classes are further combined as members of a single coincidence class. Such a design facilitates easy integration into the ROOT framework, with the class hierarchy naturally transforming to branches and sub-branches in a ROOT tree. The entire analysis suite, including the complete development history, is hosted in an online repository that is publicly viewable [26].

3.1 Coincidence Matching

With the shift in coincidence tagging from the hardware to the analysis phase of the experiment, it was necessary

to develop an algorithm that is capable of accurately identifying coincidence events in both an online and an offline environment, for all possible trigger rates. The particulars of the MIDAS system create some challenges for online identification of coincidences. In MIDAS, event data are transferred from the “frontend” VME processor to the “backend” analysis computer via a gigabit ethernet connection. For efficiency reasons, transfers are made only once per second, with events buffered locally in the VME processor in between. As a result, events from the head and the tail frontends arrive at the backend asynchronously. This is because the time of arrival is dictated by when the frontends are ready to send a packet of events, not the actual trigger time of any given event. Thus the coincidence matching algorithm must ensure that events with arrival times differing by up to two seconds can still be tagged as coincidences.

A diagram of the coincidence matching algorithm is shown in Fig. 4. Events from both the head and the tail frontend are placed into a buffer which orders the events based on their trigger time as measured by the TSC FIFO. Whenever a new event is placed into the buffer, the trigger time difference between the earliest and the latest event in the buffer is calculated. If this difference is greater than some set value (the default setting is four seconds), then the entire queue is searched for coincidence matches with the earliest event. Here, a match is defined as any two events whose timestamps are within $10 \mu\text{s}$ of each other. Regardless of whether or not a match is found, the earliest event is sent to a singles event processor which calculates all of the necessary singles parameters and sends the event on to the next stage of analysis (which is typically either histogramming, writing to disk, or both). After this, the event is removed from the buffer. If a coincidence match *is* found, the matching events are also sent to a coincidence event processor. Note that in the case of coincidences, only the earliest event is removed from the buffer. The other event will remain until it becomes the earliest event, at which time it will be analyzed as a singles event and then removed.

In practice, an `std::multiset` from the C++ standard library [27] is used as the event buffer. This container automatically maintains sorting between elements, which results in very efficient searches for coincidence matches. Furthermore, the automatic sorting naturally lends itself to checking the time difference between the earliest and the latest event in the buffer. It also allows for multiple coincidences to be stored and tagged. This is not necessary at present since the dead times render multiple coincidences (within a $10 \mu\text{s}$ window) impossible. However, it allows for easy expansion of the algorithm should multiple coincidences ever become possible. The performance of the `std::multiset` was checked against a variety of other options, including a `std::vector` and `std::deque` which are resorted after every insertion and an unordered hash container, `boost::unordered_multiset` [28]. The sorted `std::deque` performed similarly to the `std::multiset` for small objects. However, for objects the size of a real event, the additional copy operations involved in the re-

sorting reduce performance significantly. The performance of the `std::multiset` was slightly worse than the `boost::unordered_multiset` in terms of searching for coincidence matches. However, the difficulties associated with a lack of ordered elements in the latter container, as well as its reliance on non-standard libraries, do not justify the small performance increase.

3.2 Live Times

To correctly measure the yield of a reaction, it is necessary to correct the number of recorded events for the live time of the DAQ. This can be done by determining the fraction of time, L , during which the acquisition is open to new triggers. The real number of events, N , is then equal to the number of recorded events, n divided by L ,

$$N = n/L. \quad (1)$$

In conventional systems with non-paralyzable dead times, L can be determined simply from the sums of recorded scaler counts. For example, if it is possible to count the number of presented and accepted triggers, then L is simply given by

$$L = N_{\text{acq}}/N_{\text{pres}}. \quad (2)$$

In the DRAGON DAQ, there are two free-running systems with independent singles live times. For each of the singles triggers, the live time corrections can be made by the method outlined above. However, for coincidences this is not possible since coincidence tagging is performed at the analysis stage, making it impossible to count the rate of presented coincidences in a scaler alone. The lack of an available method for counting presented coincidences means that other methods must be employed to determine live time corrections. One option is to directly measure the busy time associated with each recorded event, that is, to record how long the DAQ is blind to incoming triggers on an event-by-event basis. This is part of the standard operating procedure for the IO32, which calculates the total busy time for each event from TSC measurements and stores it in the data stream. For systems with a non-paralyzable dead time response and reactions generated as a random Poisson process, the number of events lost due to dead time, n_{lost} , is given by

$$n_{\text{lost}} = \lambda \sum_{i=0}^n \tau_i = \lambda \tau, \quad (3)$$

where n is the total number of *recorded* events; λ is the rate of *generated* events; τ_i is the busy time associated with a given event i ; and τ is the sum of all busy times across a run. The number of generated events, N , over the total run time T is then given by

$$N = n + n_{\text{lost}} \quad (4)$$

$$= n + \lambda \tau \quad (5)$$

$$= n + (N/T) \tau \quad (6)$$

$$= \frac{n}{1 - \tau/T}. \quad (7)$$

From Eqn. (7), it is straightforward to calculate the number of generated events from the number of recorded events, the measured dead times, and the total run time. Alternatively, it is possible to define the live time fraction as

$$L = 1 - \tau/T \quad (8)$$

and then to use Eqn. (1) to calculate N .

For a singles analysis, τ can simply be calculated as the sum of the individual τ_i over all events. For coincidences, however, more care is required to calculate τ correctly. There are three classes of possibilities regarding the loss of coincidence events due to dead time:

1. The event arrives when neither the head nor the tail is busy: the event will be recorded and tagged as a coincidence.
2. The event arrives when either the head or the tail is busy, but not both: half of the event will be recorded and tagged as singles.
3. The event arrives when both the head and the tail are busy: the event will not be recorded at all.

In terms of correcting recorded coincidence events for dead time losses, both cases (2) and (3) should count as a loss. Thus τ should be the total time during which the *head* or the *tail* is busy (note that this is a true logical OR as opposed to the exclusive OR of case (2)). To calculate τ for coincidence events, we employ an algorithm which stores the “start” and “stop” times of all busy periods from both DAQs, sorted by their start times. The algorithm then iterates through the list, identifies any cases of overlapping head and tail busy periods, and calculates the sum of busy times with the overlaps removed.

3.2.1 Non-Poisson Events

The live time analysis presented in Eqns. (4)–(7) is only valid when the rate of generated events is a Poisson process. This is usually the case when studying nuclear reactions such as radiative capture since the underlying physics adhere to Poisson statistics. However, in beam-based experiments such as those at DRAGON, the reaction rate is governed by the underlying physics of the reaction, the rate of the incoming beam, and the target density. In cases where the beam rate (or target density) is fluctuating, the rate of occurrence of reactions becomes non-Poisson. Instead, the rate becomes an inhomogenous Poisson process, that is, one where the rate is time dependent. The expected number of events in a interval $[0, \tau]$ is then given by

$$\int_0^{\tau} \lambda(t) dt. \quad (9)$$

In an experiment, the time rate of reactions (assuming constant target density) is determined by the yield per incoming beam particle, $Y = N/N_b$, which is a constant, and incoming beam rate as a function of time, $R(t)$:

$$\lambda(t) = \frac{N}{N_b} R(t). \quad (10)$$

The number of true events, $N = n + n_{\text{lost}}$, is then

$$N = n + \sum_{i=0}^n \int_0^{\tau_i} \frac{N}{N_b} R(t) dt \quad (11)$$

$$= n + N \frac{\sum_{i=0}^n \int_0^{\tau_i} R(t) dt}{\int_0^T R(t) dt}, \quad (12)$$

or solving explicitly for N :

$$N = n \left(1 - \frac{\sum_{i=0}^n \int_0^{\tau_i} R(t) dt}{\int_0^T R(t) dt} \right)^{-1}. \quad (13)$$

From here, we can define a live time fraction analogous to that of Eqn. (2):

$$L = 1 - \frac{\sum_{i=0}^n \int_0^{\tau_i} R(t) dt}{\int_0^T R(t) dt}. \quad (14)$$

Note that if the beam rate is a constant with respect to time, $R(t) \equiv R$, we recover the definition of L given in Eqn. (8):

$$\int_0^{\tau} R(t) dt = \int_0^{\tau} R dt = R\tau \quad (15)$$

$$\Rightarrow L = 1 - \frac{\sum_{i=0}^n R\tau_i}{RT} \quad (16)$$

$$= 1 - \frac{\sum_{i=0}^n \tau_i}{T} \quad (17)$$

$$= 1 - \tau/T. \quad (18)$$

In DRAGON experiments, the beam rate is monitored continuously by measuring the rate of elastically scattered target nuclei with IIS detectors (c.f. Sect. 1.1). Thus it is possible to construct $R(t)$ from these measurements and use the full form of Eqn. (14) for live time corrections. In Sect. 4.2, we discuss the effect of including this full live time calculation in the analysis of the $^{20}\text{Ne}(p, \gamma)^{21}\text{Na}$ data reported in Ref. [29]. We show that the change in the live time after accounting for beam fluctuations is small even in the presence of substantial rate changes. However, as a general rule, the sensitivity of the final result of a measurement to higher-order live time effects will be different for each experiment. Hence the appropriate live time analysis must be considered on a case-by-case basis.

4 DAQ Commissioning Experiment

The new DRAGON DAQ was commissioned by measuring the strength of the $E_{c.m.} = 1113$ keV resonance in the $^{20}\text{Ne}(p, \gamma)^{21}\text{Na}$ radiative proton capture reaction. This reaction was also used in the original DRAGON commissioning experiment [30, 31]. Since the separator hardware has not changed appreciably since its inception, revisiting this reaction provides a reliable means to check for any inconsistencies that might be introduced by the new

DAQ. This resonance also serves as an important calibration point for measurements of direct radiative capture in $^{20}\text{Ne}(p, \gamma)^{21}\text{Na}$ at lower energies. As the starting point of the NeNa cycle, these are important for the nucleosynthesis of intermediate mass elements in ONe classical novae and the production of sodium in yellow supergiants [32, 33, 34, 35, 36].

A heavy-ion singles analysis of the DAQ commissioning experiment has already been reported in Ref. [29], with the results proving consistent with the original DRAGON commissioning. It was also shown that the commonly accepted value of the $E_{c.m.} = 1113$ keV resonance strength was incorrectly derived from a 1960 measurement [37] that was reported in the laboratory frame of reference and later misinterpreted as being in the center-of-mass frame. As shown in Ref. [29], recalculating the resonance strength of Ref. [37] in the center-of-mass frame brings it into agreement with other published measurements [30, 38]. As a result, it was recommended that the accepted value be lowered to account for this new information.

Since we have already reported the singles analysis in Ref. [29], here we focus on the coincidence aspects of the data. A summary of relevant coincidence parameters is presented in Fig. 5. Panel (a) shows the difference in trigger times for the head and tail DAQ systems, as measured by their respective IO32 TSCs. As indicated in the figure, the peak around $1.5 \mu\text{s}$ consists of true recoil events. This sits on top of a flat random background resulting from accidental coincidences between a heavy ion and an uncorrelated γ ray. Panel (b) shows the difference in trigger times as measured by the head TDC, which shows the same structure as the IO32 measurements. The inset shows the correlation between the IO32 and TDC time difference measurements. As expected, they show a near 1:1 correlation, with a slight offset due to differing signal propagation delays.

Panel (c) shows a zoomed-in view of the recoil peak in the separator TOF, which reveals additional structure. The main peak around $1.7 \mu\text{s}$ is made up of normal recoil events which are transmitted through both MCPs to the DSSSD. The small cross-hatched peak to the left of the main one consists of events in which a valid MCP0 signal is coincident with noise in MCP1. This is evidenced by looking at the relative timing of MCP0 and MCP1, which shows a random distribution of times for the MCP1 trigger relative to MCP0. The diagonal-hatched peak to the right of the main one likely consists of events which scatter in the carbon foil of MCP0 and are transmitted to MCP1 with a reduced velocity compared to unscattered recoils. These events have the same TOF from the target to MCP0 as events in the main peak, but their TOF from MCP0 to MCP1 is around 60 ns longer, and it has a significantly broader distribution compared to normal recoils. This is indicative of events which originated as normal recoils at the target and then changed velocity due to some reaction process in MCP0. For events that trigger off the MCPs (as opposed to the DSSSD), the MCP1 signal defines the trigger, so as a result the separator TOF is taken relative to MCP1. This means that any delay in MCP1 timing

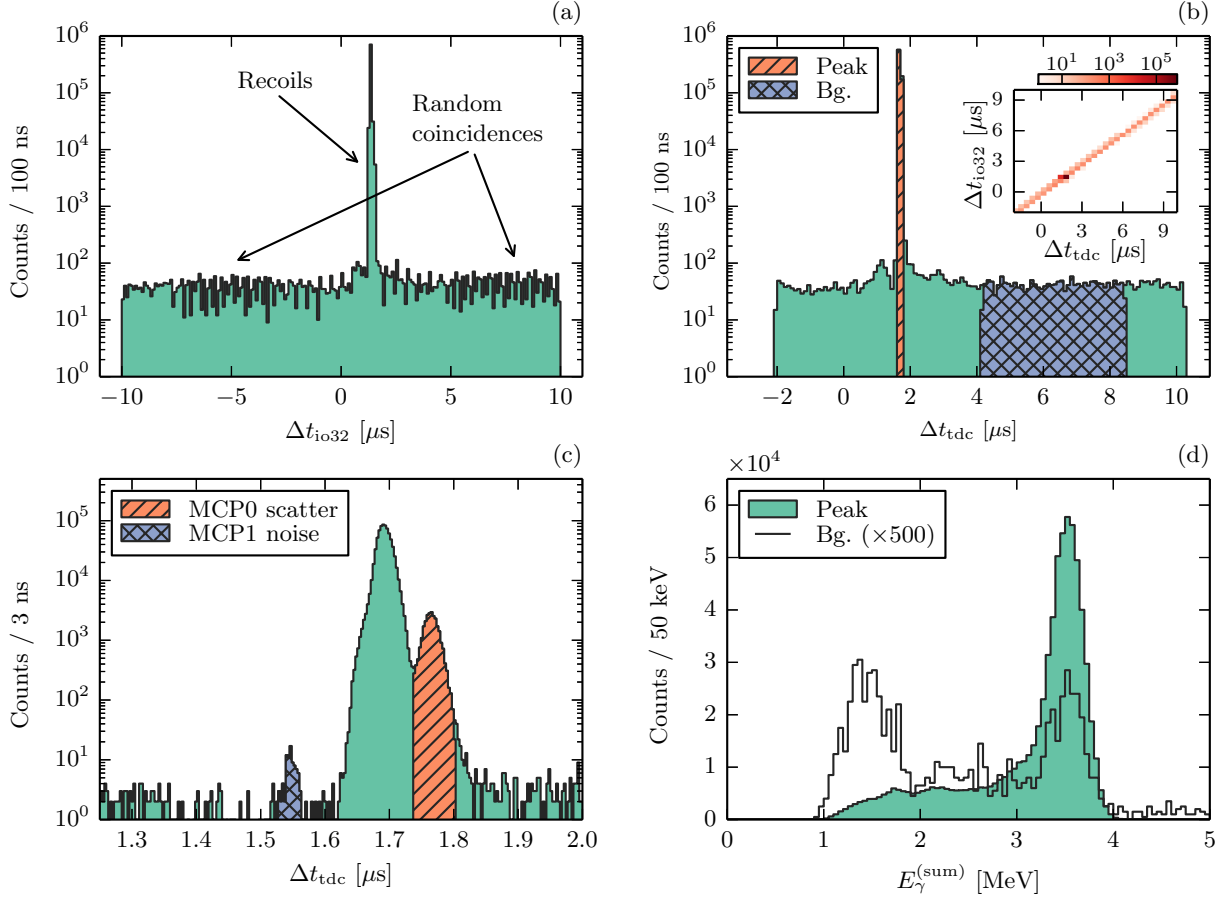


Fig. 5. Panel (a): difference in trigger times (tail minus head) as measured by the IO32 TSC. Panel (b): difference in trigger times as measured by the head TDC, with the hatched regions denoting cuts applied to the spectra in Panel (d). The inset shows the correlation between the IO32 and TDC trigger time difference measurements. Panel (c): close up of the recoil peak region of the TOF spectrum. The structure of the peaks and the meaning of the hatched regions are discussed in the text. Panel (d): sum of coincidence γ -ray energies measured in the BGO array. The shaded histogram consists of events from the recoil peak in separator TOF (diagonal-hatched region in Panel (b)), while the unshaded histogram is composed of an arbitrary background region (cross-hatched region in Panel (b)).

due to recoils changing velocity in MCP0 will manifest as a delay in the separator TOF by the same amount, which is the case for events in the cross-hatched peak. Furthermore, the cross-hatched events do not come with a valid signal in the DSSSD as would be expected for recoils which scatter and change their trajectory to one outside the DSSSD acceptance.

Panel (d) in Fig. 5 shows the BGO γ -ray energy sum for events in the recoil peak (shaded histogram) superimposed with events from an arbitrary background region outside the recoil peak (unshaded histogram). As expected, the recoil γ rays are almost all concentrated in a strong peak at the 3.5 MeV decay energy of the state populated in the reaction. The background histogram, on the other hand, has a significant enhancement near threshold resulting from room background γ -rays.

4.1 Resonance Strength Calculation

To verify that the timestamp-based coincidence matching is working as intended, we have performed a full coincidence analysis of the $E_{c.m.} = 1113$ keV resonance strength in $^{20}\text{Ne}(p, \gamma)^{21}\text{Na}$, using data taken during the DAQ commissioning experiment. The details of the experiment and the resonance strength calculation, including the employed stopping power, are identical to Ref. [29]. However, the recoil event selection and overall efficiency are different in the present analysis. A summary of the recoil event selection is shown in Fig. 6. The final recoil cut is an AND of the DSSSD energy cut used in Ref. [29], a cut on the recoil peak in separator TOF, and a cut on the energy deposited by the most energetic γ -ray.

Table 1 shows a summary of the detection efficiency, yield, and resonance strength in the coincidence analysis. The detection efficiency differs from that of Ref. [29]

in two ways: the live time is different as a result of the coincidence trigger requirement, and the γ -ray detection efficiency becomes part of the total efficiency product. The live time was calculated using Eqn. (8), with the total dead time τ being the logical OR of dead times in the head and tail systems, as explained in Sect. 3.2. The uncertainty on the live time is equal to the 20 parts per million accuracy rating of the IO32 quartz crystal, i.e. a *relative* uncertainty of 0.002%. The BGO efficiency was calculated from a GEANT3 simulation [39], with the branching ratios for the decay of the 3.54 MeV state in ^{21}Na taken from Ref. [40]. The simulated events were analyzed with the same energy cut as the data:

$$1.1 \text{ MeV} < E_{\gamma}^{(\text{max})} < 4.5 \text{ MeV},$$

where $E_{\gamma}^{(\text{max})}$ is the energy deposited by the most energetic γ ray. This accounts for any effect of hardware thresholds since the lower limit of 1.1 MeV is beyond the range of the threshold function. The uncertainty on the BGO efficiency calculation was estimated at 10% as explained in Ref. [39].

We have also assigned an uncertainty of 3% to the gas target transmission. This was estimated from the standard deviation of Faraday cup readings taken upstream and downstream of the gas target. Each set of readings sampled the beam current approximately every 0.2 s over the course of 30 s. This transmission uncertainty was not included in the singles analysis of Ref. [29]. In Table 1 we also report the updated singles yield and resonance strength when including the 3% gas target transmission uncertainty in the calculation. The overall effect is minor, appearing only in the last quoted digit of the uncertainty on the resonance strength.

As indicated in Table 1, the present yield and resonance strength are in very good agreement with the singles values, as well as the measurements of Refs. [30, 37, 38] (with the appropriate center-of-mass corrections made to Ref. [37]). Note that the increased uncertainty on the coincidence yield and resonance strength as compared to their singles counterparts is a consequence of the 10% uncertainty attached to the BGO efficiency.

4.2 Live Time Analysis

The rate of the incoming ^{20}Ne beam varied significantly throughout the course of the DAQ commissioning experiment. This is because the beam was extracted from the ISAC offline microwave ion source [41], which requires passing the beam through a stripper foil to reach a charge state suitable for acceleration. Degradation of stripper foils resulted in steady decreases in beam intensity on the time scale of a few hours, after which the ISAC operators would replace the foil and return the beam intensity to its initial state. As a result, the present data set provides an ideal case to examine the effect of varying beam rates on the live time calculations.

To examine the effect of varying beam rates on the live time, we calculated heavy-ion *singles* live times on a

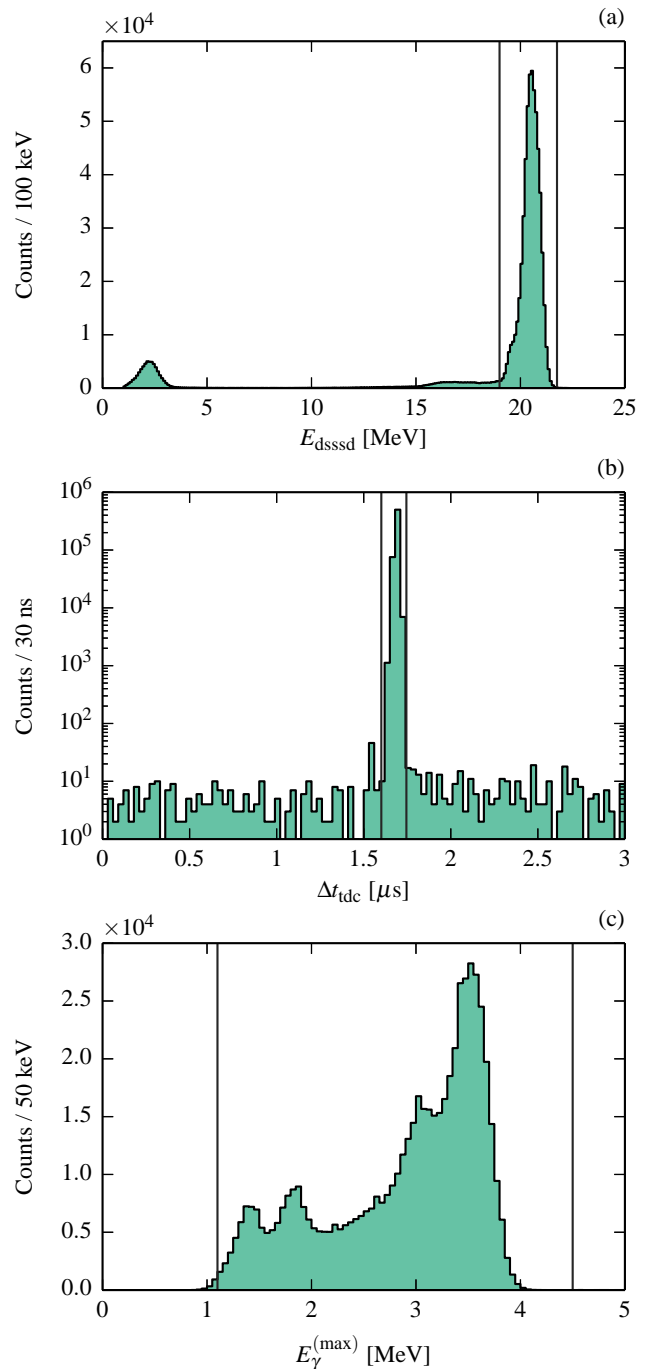


Fig. 6. Summary of cuts used in the coincidence resonance strength analysis. Panel (a): DSSSD energy cut; Panel (b): separator TOF cut on the prompt recoil peak; and Panel (c): cut on the energy deposited by the most energetic γ -ray. In each panel, the cut limits are indicated by vertical lines. The final recoil cut is an AND of all three conditions. All histograms consist of coincidence events only, and those in Panels (b) and (c) consist only of events which pass the cuts shown in the panels above them.

Table 1. Summary of the coincidence yield calculation. Quantities which are different from or supplementary to those in Ref. [29] are labeled in bold face. The table also includes the singles yield and resonance strength, with the uncertainties on these quantities updated relative Ref. [29]. They now include propagation of the 3% uncertainty on the gas target transmission.

Quantity	Value
DSSSD detection efficiency [15]	$97.0 \pm 0.7\%$
Ne ⁽⁹⁺⁾ charge state fraction [30]	$59 \pm 1\%$
DRAGON transmission [31]	$99.9^{+0.1}_{-0.2}\%$
MCP transmission [14]	$76.9 \pm 0.6\%$
Gas target transmission	$94 \pm 3\%$
Coincidence live time	$91.486 \pm 0.002\%$
BGO detection efficiency	$55.9 \pm 10.0\%$
Total coincidence efficiency	$21.1 \pm 3.9\%$
Integrated beam current	$(2.296 \pm 0.032) \times 10^{15}$
Detected recoils	$(5.923 \pm 0.062) \times 10^5$
Yield	$(1.221 \pm 0.221) \times 10^{-9}$
Resonance strength	0.969 ± 0.210 eV
Singles yield	$(1.225 \pm 0.051) \times 10^{-9}$
Singles resonance strength	0.972 ± 0.119 eV

run-by-run² basis using three different methods. The first method (“Poisson”) calculates the live time from the total sum of busy times divided by the total run time, as represented by Eqn. (8). This method was employed both in the present coincidence resonance strength calculation (Sect. 4.1) and the singles result reported in Ref. [29]. The second method (“scaler”) uses the ratio of acquired to presented triggers measured by the IO32 scalers, viz. Eqn. (2). The third method (“non-Poisson”) involves treating the trigger rate as an inhomogeneous Poisson process as outlined in Sect. 3.2.1. For this method, we treat the incoming beam rate, $R(t)$, as being proportional to the IIS trigger rate, $R_{\text{iis}}(t)$. The proportionality constant cancels out in Eqn. (14), so we can set $R(t) \equiv R_{\text{iis}}(t)$. To evaluate Eqn. (14) from the measured IIS rates, we divide each run into 30 second periods. For each period j we treat the rate as being a constant R_j equal to the average IIS rate over the period. To evaluate the integrals over $R(t) dt$, we use a simple rectangle method with one second bin sizes. Expressed mathematically, our approximation to Eqn. (14) is

$$L \simeq 1 - \frac{\sum_{j=0}^{n_j} R_j \sum_{i: \tau_i \in S_j} \tau_i}{\sum_{i=0}^{n_i} R_i \Delta}, \quad (19)$$

where the index i corresponds to the one second bins used for integral evaluation; Δ is equal to one second; n_i is the number of one-second divisions per run, i.e. T/Δ ; R_i is the measured IIS rate during each bin i ; and τ_i is the sum of measured busy times within the bin i . The index j is over the 30 second periods during which we treat the IIS rate as constant, and n_j is the number of 30 second periods

per run. S_j is the time interval corresponding to a period j , i.e. the range $t_j \leq t \leq t_j + 30$ s where t_j denotes the start of the period j . Finally, R_j is the average IIS rate over a division j :

$$R_j \simeq \frac{\sum_{k: t \in S_j} R_k \Delta}{\sum_{k: t \in S_j} \Delta}. \quad (20)$$

The results of the live time analysis are shown in Fig. 7, along with the IIS trigger rate as a function of time. The figure presets the scaler and non-Poisson live times as ratios to the Poisson live time, L_0/L' , where L_0 is the Poisson live time and L' is either the scaler or non-Poisson live time. This represents the fractional change in the yield that would result from using either the scaler or non-Poisson live time instead of the Poisson. The scaler and non-Poisson live times agree well with each other. For the runs with the most significant rate fluctuations, they trend towards being slightly lower than the Poisson live time (resulting in a higher L_0/L' ratio) but still differ by no more than 1.5%. We have also calculated live times across the entire experiment, L_{full} , by taking the weighted average of the inverse of the run-by-run live times with the weights being the number of recoils detected:

$$L_{\text{full}} = \left(\frac{\sum_i n_{r,i}/L_i}{\sum_i n_{r,i}} \right)^{-1}. \quad (21)$$

Calculated this way, correcting the total sum of detected recoils using L_{full} is the mathematical equivalent of making live time corrections run-by-run, i.e.

$$\sum_i \frac{n_{r,i}}{L_i} = \frac{\sum_i n_{r,i}}{L_{\text{full}}}. \quad (22)$$

The respective L_{full} values for the Poisson, scaler, and non-Poisson methods are 95.6%, 94.8%, and 94.9%. These translate to fractional yield changes ($Y'/Y_0 - 1$) of 0.86% and 0.71% for the scaler and non-Poisson methods, respectively. We have also calculated the non-Poisson live time for the coincidence measurement presented in Sect. 4.1, arriving at an overall live time of 90.7%, which translates to a fractional yield change of 0.91%. Such changes are small compared to the overall error budget. Since the present analysis represents a particularly extreme case of beam rate fluctuations, this can be taken as an indication that the final result of a DRAGON experiment is not likely to be sensitive to the particular method of live time calculation.

5 Conclusions

In conclusion, we have developed a new DAQ for the DRAGON recoil mass separator at TRIUMF. The new DAQ consists of two free-running acquisition systems with completely independent triggering and readout, one for the γ -ray detectors surrounding the target and the other for heavy-ion detectors at the end of the separator. Events are recorded with timestamps from a local 20 MHz clock,

² Each run represents ~ 1 hour of data taking bookended by Faraday cup readings.

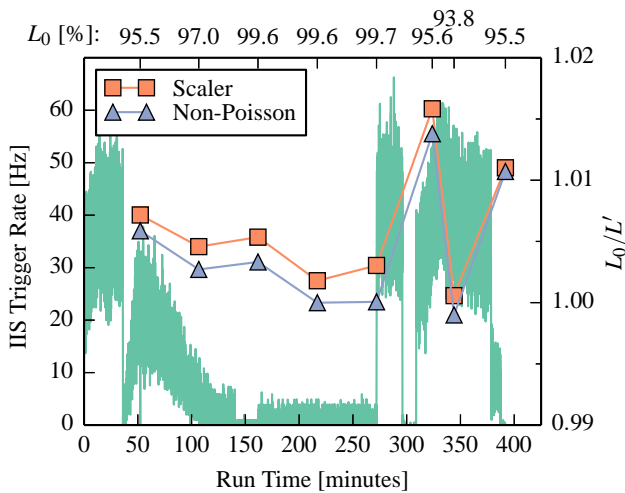


Fig. 7. Effect of beam fluctuations on the heavy-ion singles live time calculations. The solid histogram shows the IIS trigger rate as a function of time. The filled squares and triangles denote the ratio of live times L_0/L' , where L_0 is the live time calculated using Eqn. (8) and L' is the live time calculated using an alternative method. The alternative methods are the “scaler” method (squares) using Eqn. (2) and the “non-Poisson” method (triangles) using Eqn. (14). The horizontal positions of the markers denote the end times of runs throughout the experiment. The run-by-run live times calculated using the Poisson method are also displayed textually across the top of the figure.

with the clock frequencies and zero-point offsets synchronized between the two systems. Comparison of timestamp values allows coincidence events to be identified in the first stage of data analysis, and we have implemented and successfully employed a coincidence-matching algorithm that is suitable for both online and offline analysis.

The new DRAGON DAQ was commissioned by measuring the strength of the $E_{c.m.} = 1113$ keV resonance in the $^{20}\text{Ne}(p,\gamma)^{21}\text{Na}$ radiative capture reaction. The experiment ran successfully, and the measured coincidence resonance strength, $\omega\gamma = 0.969 \pm 0.210$ eV, is in good agreement with our previous singles result [29], as well as earlier publications [30, 37, 38]. All activities to date indicate that the DAQ upgrade is successful and that the new system can be used in future DRAGON experiments.

6 Acknowledgements

We are grateful to the ISAC operations and offline ion source groups for delivery of a high quality ^{20}Ne beam during the DAQ commissioning experiment. We also thank P. Amadruz for his guidance and efforts in developing the new DAQ system. This work was supported in part by the National Research Council and National Sciences and Engineering Research Council of Canada.

References

1. C. Akers *et al.*, *Phys. Rev. Lett.* **110**, 262502 (2013).
2. A. L. Sallaska, C. Wrede, A. García, D. W. Storm, T. A. D. Brown, C. Ruiz, K. A. Snover, D. F. Ottewell, L. Buchmann, C. Vockenhuber, D. A. Hutcheon, and J. A. Caggiano, *Phys. Rev. Lett.* **105**, 152501 (2010).
3. L. Erikson *et al.*, *Phys. Rev. C* **81**, 045808 (2010).
4. C. Ruiz *et al.*, *Phys. Rev. Lett.* **96**, 252501 (2006).
5. S. Bishop *et al.*, *Phys. Rev. Lett.* **90**, 162501 (2003).
6. J. Fallis *et al.*, *Phys. Rev. C* **88**, 045801 (2013).
7. C. Vockenhuber *et al.*, *Phys. Rev. C* **76**, 035801 (2007).
8. J. DAuria *et al.*, *Phys. Rev. C* **69**, Art. No. 065803 (2004).
9. B. Davids, R. H. Cyburt, J. Jos, and S. Mythili, *Astrophys. J.* **735**, 40 (2011).
10. C. Matei *et al.*, *Phys. Rev. Lett.* **97**, 242503 (2006).
11. D. Schürmann, A. D. Leva, L. Gialanella, R. Kunz, F. Strieder, N. D. Cesare, M. D. Cesare, A. D’Onofrio, K. Fortak, G. Imbriani, D. Rogalla, M. Romano, and F. Terrasi, *Phys. Lett. B* **703**, 557 (2011).
12. D. Hutcheon *et al.*, *Nucl. Instr. Meth. in Phys. Res. A* **498**, 190 (2003).
13. R. Laxdal, *Nucl. Instr. Meth. in Phys. Res. B* **204**, 400 (2003).
14. C. Vockenhuber, L. Erikson, L. Buchmann, U. Greife, U. Hager, D. Hutcheon, M. Lamey, P. Machule, D. Ottewell, C. Ruiz, and G. Ruprecht, *Nucl. Instr. Meth. in Phys. Res. A* **603**, 372 (2009).
15. C. Wrede, A. Hussein, J. G. Rogers, and J. DAuria, *Nucl. Instr. Meth. in Phys. Res. B* **204**, 619 (2003).
16. A. Simon, J. Fallis, A. Spyrou, A. M. Laird, C. Ruiz, L. Buchmann, B. R. Fulton, D. Hutcheon, L. Martin, D. Ottewell, and A. Rojas, *Eur. Phys. J. A* **49**, 1 (2013).
17. K. Olchanski, *VME-NIMIO32 - General Purpose VME FPGA Board*, Tech. Rep. (TRIUMF, Vancouver, BC Canada, 2012).
18. *Cyclone Device Handbook*, Tech. Rep. (Altera Corporation, San Jose, CA USA, 2008).
19. *Model V1190-VX1190 A/B, 128/64 Channel Multi-hit TDC*, Tech. Rep. (CAEN S.p.A., Viareggio, Italy, 2012).
20. *Model V792/V792N, 32/16 Channel QDC*, Tech. Rep. (CAEN S.p.A., Viareggio, Italy, 2010).
21. *Model V812 16 Channel Constant Fraction Discriminator*, Tech. Rep. (CAEN S.p.A., Viareggio, Italy, 2011).
22. *Model V785, 16/32 Channel Peak Sensing ADC*, Tech. Rep. (CAEN S.p.A., Viareggio, Italy, 2012).
23. S. Ritt and P. Amadruz, in *Proc. of the Xth IEEE REAL TIME Conference* (1997) pp. 309–312, see also <http://midas.psi.ch>.
24. “Daq related information site,” <http://daq-plone.triumf.ca/> (2012), accessed: 2013-11-25.
25. R. Brun and F. Rademakers, *Nucl. Instrum. Meth. in Phys. Res. A* **389**, 81 (1997), see also <http://root.cern.ch>.

26. “DRAGON analysis codes,” <https://github.com/dragontriumf/analyzer/> (2014), accessed: 2014-02-20.
27. N. M. Josuttis, *The C++ Standard Library: A Tutorial and Reference*, 2nd ed. (Addison Wesley Longman, Upper Saddle River, NJ USA, 2012).
28. J. Maddock, “Boost TR1,” http://www.boost.org/doc/libs/1_55_0/doc/html/boost_tr1.html (2005), accessed: 2013-11-25.
29. G. Christian, D. Hutcheon, C. Akers, D. Connolly, J. Fallis, and C. Ruiz, *Phys. Rev. C* **88**, 038801 (2013).
30. S. Engel *et al.*, *Nucl. Instr. Meth. in Phys. Res. A* **553**, 491 (2005).
31. S. Engel, *Awakening of the DRAGON: Commissioning of the DRAGON recoil separator facility and first studies on the $^{21}\text{Na}(\alpha, p)^{22}\text{Mg}$ reaction*, Ph.D. thesis, Ruhr-Universität Bochum, Bochum, Germany (2003), unpublished.
32. C. Rolfs, W. Rodne, M. Shapiro, and H. Winkler, *Nucl. Phys. A* **241**, 460 (1975).
33. J. José, A. Coc, and M. Hernanz, *Astrophys. J* **520**, 347 (1999).
34. N. Prantzos, A. Coc, and J. P. Thibaud, *Astrophys. J* **379**, 729 (1991).
35. R. Bloch, T. Knellwolf, and R. Pixley, *Nucl. Phys. A* **123**, 129 (1969).
36. C. Iliadis, R. Longland, A. Champagne, A. Coc, and R. Fitzgerald, *Nucl. Phys. A* **841**, 31 (2010).
37. G. C. Thomas and N. W. Tanner, *Proc. Phys. Soc.* **75**, 498 (1960).
38. J. Keinonen, M. Riihonen, and A. Anttila, *Phys. Rev. C* **15**, 579 (1977).
39. D. G. Gigliotti, *Efficiency calibration measurement and GEANT simulation of the DRAGON BGO gamma ray array at TRIUMF*, Master’s thesis, University of Northern British Columbia, Prince George, Canada (2004), unpublished.
40. R. Firestone, *Nuclear Data Sheets* **103**, 269 (2004).
41. K. Jayamanna, F. Ames, G. Cojocaru, R. Baartman, P. Bricault, R. Dube, R. Laxdal, M. Marchetto, M. MacDonald, P. Schmor, G. Wight, and D. Yuan, *Rev. Sci. Instr.* **79**, 02C711 (2008).